Hindawi
Journal of Computer Networks and Communications
Volume 2023, Article ID 4297044, 9 pages
https://doi.org/10.1155/2023/4297044

Research Article

Analysis of 5G Smart Communication Base Station Doppler-Smoothed Pseudorange Single-Point Geodesic Positioning Accuracy

Jianmin Wang and Yan Wang

School of Geomatics, Liaoning Technical University, Liaoning 123000, Fuxin, China

Correspondence should be addressed to Jianmin Wang; wangjianmin@lntu.edu.cn

Received 5 September 2022; Revised 4 October 2022; Accepted 15 October 2022; Published 22 February 2023

Academic Editor: Arvind Kumar

With the continuous development of mobile communication and satellite navigation technologies, the positioning requirements of 5G smart communication base stations are becoming higher and higher. With the opening of GNSS raw observation data, research on the positioning of a 5G smart communication base station has become a research hotspot in the surveying and mapping disciplines. In this paper, based on the GNSS observation data of the 5G smart communication base station, the quality of the original GNSS observation data of the 5G smart communication base station is studied and analyzed. A method based on Doppler smoothing pseudorange solves the problem that the original pseudorange observation values of the 5G smart communication base station are noisy and prone to multipath errors due to the limitations of the base station chips and processes, which makes the traditional data processing methods unable to meet the demand for higher accuracy positioning. This method uses Doppler observations to smooth the pseudorange and determines the Doppler smoothing strategy and closure values to improve the data quality. The experimental data show that Doppler smoothing pseudorange can improve data quality and positioning accuracy by 67.9% in the *E* direction, 64.8% in the *N* direction, and 65.5% in the *U* direction. The future world will develop in the direction of intelligence, and the wireless network 5G technology used to support the construction of this intelligent system will become the core driver for the development of a leading intelligent society. 5G network signals have higher reliability and lower latency and can meet the specific needs of smart manufacturing, autonomous driving, and other industrial applications. This new base station product can meet the construction needs of future 5G base stations, adapt to the future intensive, miniaturized, intelligent station construction mode, and realize safe and fast station construction, providing the necessary hardware support for 5G network coverage.

1. Introduction

Currently, the global navigation satellite system (GNSS) technology is developing rapidly, providing all-weather, high-precision navigation and positioning services to different members of society. The successful launch of the 55th BeiDou navigation satellite marked the full deployment of the BeiDou navigation satellite system (BDS) constellation in China [1, 2]. With the continuous development of mobile communication and satellite navigation technologies, mobile intelligent terminals have been widely used in the fields of location sharing, engineering measurement, pedestrian navigation, firefighting, and disaster mitigation. In daily life, how to obtain real-time and high-precision geographic location information through mobile smart terminals has become a popular topic, and people have an increasing demand for smart terminal positioning [3, 4]. Especially since 2016, Google has provided interfaces to obtain raw GNSS observations (such as C1 pseudorange observation, and L1 carrier phase observation, D1 Doppler observation) in its Android Nougat 7.0 and above operating system for mobile devices, but due to the influence of the smart terminal chip process and antenna, the observation noise and multipath error are large when positioning at the base station [5, 6]. However, due to the influence of the smart terminal chip process and antenna, the observation noise and multipath error during base station positioning are large, resulting in low positioning accuracy, so how to improve the positioning accuracy of smart devices has become a research hotspot in recent years [7, 8].

Doppler observation has better observation accuracy and is not easily disturbed by multipath errors [9, 10]. The study [11] analyzed the difference between multipath errors in 5G smart communication base station and geodetic receivers. A study [12] showed that using Doppler combined with pseudorange observation for localization is better than using pseudorange observation alone. The study [13] investigated the feasibility of Doppler smoothing pseudorange. The study [14] used Doppler observations for pseudorange smoothing to improve the accuracy and stability of localization. Since the antennas of 5G smart communication base stations are different from those of geodetic receivers, 5G smart communication base stations are more likely to track satellite signals, but the signal-to-noise ratio is lower than that of geodetic receivers, and the multipath effect of 5G smart communication base stations is an order of magnitude higher than that of geodetic receivers [15, 16]. This is one of the main reasons for the poor positioning accuracy of 5G smart communication base stations, and these research works have been done by many scholars and will not be discussed here [17, 18].

To address the problem of low positioning accuracy of 5G smart communication base stations, this paper makes full use of the feature that Doppler observations are not affected by multiple paths to carry out research on the application of Doppler observation smoothing pseudorange for smart terminals, carries out research on coarse difference rejection and broad value setting in the process of Doppler smoothing, and preprocesses measurement data according to the analysis results to achieve the purpose of improving positioning accuracy [19, 20].

2. Doppler Positioning Architecture

The target positioning method of a single satellite is as follows: acquire the coordinates of the satellite's hypostasis; acquire the incoming wave direction angle of the target and the zenith angle from the satellite to the target; establish the first spherical triangle on the Earth's surface with the hypostasis, the target, and the pole as the vertices; the pole is the South Pole of the Earth or the North Pole of the Earth; determine the coordinates of the target B and the pole N based on the relationship between the sides and angles of the first spherical triangle. Based on the coordinates of the first spherical triangle, the coordinates of the substar point A, the incoming wave direction angle, and the sky bottom angle, the position of the target B and the pole N are determined. Based on the position of the target B and the pole N, the coordinates of the target B are determined. When the satellite flies over the target radiation source, the single-satellite positioning process is carried out, and its radius l acceleration changes continuously during the motion. Based on the correspondence between the radial acceleration and the target position, the radial acceleration of the target is measured at several moments, and then combined with the constraint of the target position on the Earth, the coordinates of the radiation source position can be located (see Figure 1).

STK (Satellite Tool Kit), or Satellite Simulation Kit, was developed by AGI, USA, to quickly and effectively analyze missions in complex environments such as land, sea, and air, and to support the whole process of space missions, including design, test, launch, operation, and mission. Therefore, it is widely used in the aerospace industry and in science and technology fields. In this paper, we choose the STK version 10 environment and build a motion scenario including a ground radiation source, motion satellite, and on-board receiver with the powerful and realistic analysis capability of STK. The communication simulation module of STK is used to analyze the reception of ground radiation source signals by the on-board receiver. The simulation flow of single-star passive positioning is shown in Figure 2.

Positioning based on Doppler information mainly refers to the use of Doppler frequency and Doppler frequency change rate to determine the positioning surface, multiple measurements to obtain multiple positioning surfaces, and intersection position as the target's positioning point. Generally, the target is on Earth's surface or at a relatively low height, and two-dimensional plane analysis is used. As shown in Figure 3.

3. Coarse Difference Detection and Doppler Smoothing Algorithm

GNSS pseudorange observations contain various errors caused by observation equipment, propagation paths, relativity, satellite ephemeris, etc. Therefore, the single-point positioning results are affected by satellite ephemeris errors and atmospheric refraction errors. Due to the influence of the 5G smart communication base station itself, the measurement results are not as stable as those of earth-based receivers, and the observations contain large, coarse differences. By using pseudorange observations for real-time dynamic positioning, we can avoid the problems of resolving ambiguity and dealing with circular jumps, and the accuracy of the obtained positioning results can meet the single-solution needs of most navigation users. However, pseudorange observation is susceptible to multipath effects, nonvisual distance, and signal occlusion, which makes dynamic localization using pseudorange in complex scenarios less effective. Due to the effect of the duty cycle, it is difficult for intelligent terminals to obtain ideal carrier phase observations, so Doppler observations can be used to smooth the pseudorange and improve the satellite positioning accuracy of intelligent terminals. When there is no duty cycle limitation, the smoothed pseudorange of carrier phase observation can obtain more reliable satellite positioning results from the smart terminal. In this paper, we detect ephemeris elements containing coarse differences by calculating quadratic differences between ephemeris elements, removing the ephemeris elements, and restarting the smoothing calculation.

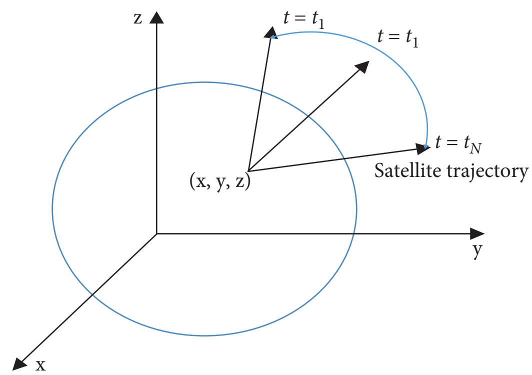

Figure 1: Schematic diagram of a single-star passive positioning model.

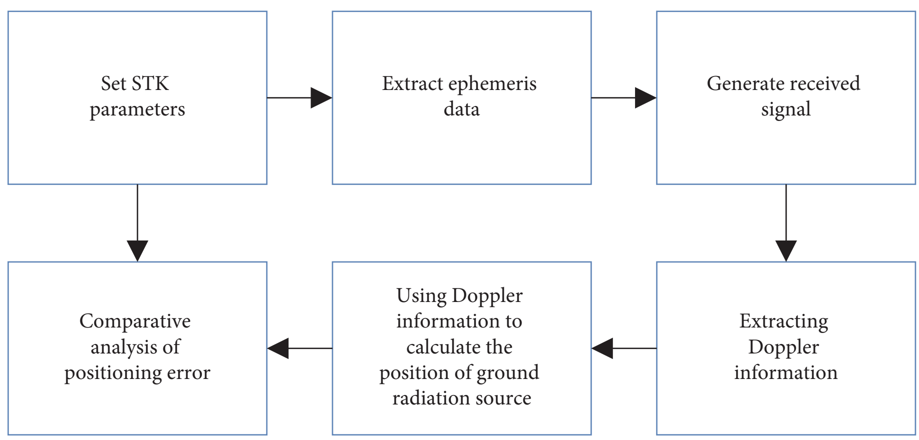

Figure 2: Single-star passive positioning simulation flow chart.

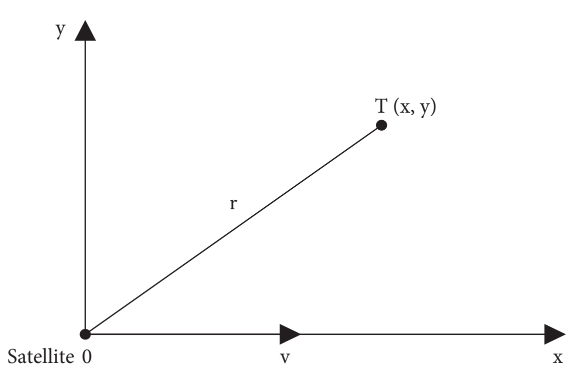

Figure 3: Schematic diagram of a planar motion scene.

For the calendar element k, the pseudorange observation equation can be expressed as the following equation:

$$\rho_k^s = R_k^s + c\delta t_k - c\delta t_k^s + \delta\rho_{k,\mathrm{trop}}^s + \delta\rho_{k,\mathrm{ion}}^s + \delta\rho_{k,\mathrm{rel}}^s + \delta\rho_{k,\mathrm{sagnc}}^s + \varepsilon_{\rho,k}^s. \quad (1)$$

where s is satellite number; c is the speed of light; ρ_k^s is the pseudorange observation; R_k^s is true satellite ground distance from the receiver; δt_k is the receiver clock difference; δt_k^s is the satellite clock difference; $\delta\rho_{k,\mathrm{trop}}^s$, $\delta\rho_{k,\mathrm{ion}}^s$ are tropospheric delay error and ionospheric delay error; $\delta\rho_{k,\mathrm{rel}}^s$ is the relativistic effect; $\delta\rho_{k,\mathrm{sagnc}}^s$ is the Earth's rotation error; $\varepsilon_{\rho,k}^s$ is the unmodeled error such as multipath and measurement noise.

The single difference between epoch $k+1$ and epoch k of (1) can eliminate or weaken the effects of tropospheric delay error, ionospheric delay error, relativistic effect, and Earth rotation error. Since the satellite clock is more stable, the single difference between pseudorange ephemeris elements is a smooth curve when no large jump occurs in the receiver clock. Then, the double difference between the ephemeris is a straight line tending to 0. According to error theory, (an error is an experimental scientific term that refers to the extent to which the measurement results deviate from the true value. Mathematically, the measured value or other approximate value and the difference between the true value of the error. The error theory is the study of the error in the experiment of a theory; error theory is the test technology, instrumentation, and engineering experiments and other fields' indispensable and important theoretical basis; it plays an important role in science and production practice.) Three times, a medium error is selected as the limit difference for coarse difference rejection.

Because of the increased more week-hopping of 5G smart communication base station carrier phase observations, the pseudorange smoothing effect is not good, so this paper uses Doppler smoothing pseudorange, which is not affected by week-hopping and whose algorithm is more efficient, and base station Doppler smoothing pseudorange is derived from carrier phase smoothing pseudorange.

For the calendar element k, the carrier phase observation equation can be expressed as the following equation:

$$\varphi_k^s = R_k^s + c\delta t_k - c\delta t_k^s + \delta\rho_{k,\mathrm{trop}}^s - \delta\rho_{k,\mathrm{ion}}^s + \delta\rho_{k,\mathrm{rel}}^s + \delta\rho_{k,\mathrm{sagnc}}^s - \lambda N^s + \varepsilon_{\varphi,k}^s, \tag{2}$$

where φ_k^s is the carrier phase observation; λ is the corresponding carrier wavelength; N^s is the whole-period ambiguity; $\varepsilon_{\varphi,k}^s$ is the unknown carrier phase measurement noise; rest parameters have the same meaning as equation (1).

In the initial epoch, let the initial smoothing pseudorange be equal to initial epoch pseudorange observation, i.e., $\overline{\rho}_k = \rho_k$, then the conventional equation of carrier smoothing pseudorange is in the following equation:

$$\overline{\rho}_{k+1} = \omega_{k+1}\rho_{k+1} + \left(1 - \omega_{k+1}\right)\left(\overline{\rho}_k + \varphi_{k+1} - \varphi_k\right), \tag{3}$$

where the first coefficient on the right side of the equation $\omega_{k+1} = 1/(K+1)$ is usually called the weighted smoothing factor, which is equivalent to the following equation:

$$\overline{\rho}_{k+1} = \omega_{k+1}\sum_{i=1}^{k}\rho_i + \omega_{k+1}\sum_{i=1}^{k}\left(\varphi_{k+1} - \varphi_i\right). \tag{4}$$

Combining equations (2)–(4), it can be seen that the use of carrier smoothing pseudorange is independent of whole-period ambiguity, and the result obtained from $\varphi_{k+1} - \varphi_k$ is a high-precision pseudorange change rate, while a high-precision pseudorange change rate can be directly obtained in the 5G smart communication base station.

According to a white paper published by the European GNSS Agency (GSA), Doppler observations are derived from pseudorange rates of change, and the relationship is given in the following equation:

$$\mathrm{PsdR} = -\alpha \times \mathrm{Dopplershift}, \tag{5}$$

where PsdR denotes the pseudorange variation rate, whose value can be obtained from Google's open GNSS raw data API interface; α is a constant, which can be expressed as $\alpha = c/f_i$; c is the speed of light; f_i is the central frequency of the signal (e.g., $L1 = 1575.42\mathrm{e}6$ Hz); and Doppler shift is the Doppler observation value.

Because Doppler observations have better observation accuracy and are not disturbed by multipath errors, the relationship between pseudorange change rate and Doppler observations can be known from equation (5), and pseudorange change rate PsdR is used instead of $\varphi_{k+1} - \varphi_k$ for pseudorange smoothing in cell phone Doppler smoothing pseudorange, which can be expressed as the following equation:

$$\overline{\rho}_{k+1} = \omega_{k+1}\rho_{k+1} + \left(1 - \omega_{k+1}\right)\left(\overline{\rho}_k + \mathrm{PsdR}\right). \tag{6}$$

4. Results

Due to the high power consumption of GNSS modules in long-term continuous operation, 5G smart communication base station manufacturers have introduced a "duty cycle" mechanism within the base station to ensure the low power consumption of the GNSS module, which causes discontinuous carrier phase tracking, resulting in circular jumps in the phase observations of the front and rear ephemeris. The base station can turn on the option to force full tracking of GNSS measurements to eliminate the effect of the "duty cycle." Table 1 shows the fields of raw observations available for 5G smart communication base stations.

Before pseudorange smoothing, data are first preprocessed to detect jumps between Doppler and pseudorange observations by making a primary difference between observed Doppler and pseudorange values and then a second difference between epochs to determine a reasonable reading value. Table 2 shows an error in the double-difference value of an observable satellite.

From Table 2, we can see that the Doppler observation data are relatively stable, and the double difference can reflect that some satellites contain coarse differences while the pseudorange observation data vary more through the double difference, so it is easy to find the coarse differences through the double difference and eliminate them. Obviously, G11 and G32 are normal observations because the observation epoch of the G11 satellite is relatively small, so satellite 32 is selected as a reference, and 0.9 Hz (3 times the medium error) is set as the reading value of the Doppler double difference and 15 m (3 times the medium error) is set as the ranking value of the pseudorange double difference.

The satellites G11, G32, G22, and G23 are selected for detailed analysis, where G11 and G32 are normal observations without jump, and the single and double differences of the observed satellite Doppler and pseudorange observations are observed and calculated by epoch elements, and the comparison results are shown in Figure 4.

Figure 4 shows single and double differences between Doppler and pseudorange observations of the G11 satellite, calendar element by calendar element. It can be seen that Doppler observations contain small jumps, while pseudorange observations do not have jumps. 99.5% of the absolute values of single differences between Doppler observations are within 2 Hz, and 985% of the absolute values of double differences between ephemerides are within 1 Hz. The single difference between calendar elements of the pseudorange observation value varied smoothly, and the absolute value of the double difference between calendar elements did not exceed 15 m. Figure 4 reflects variation rate of Doppler and pseudorange variation when a 5G smart communication base station tracks satellites normally, which provides data support for setting coarse difference rejection broad value.

Figure 5 shows single and double differences between Doppler and pseudorange observations of the G32 satellite, calendar element by calendar element. It can be seen that Doppler observations contain small jumps, while pseudorange observations do not have jumps. 99.9% of the absolute values of single differences between Doppler observations and double differences between ephemerides are within 2 Hz, and 98.6% of the absolute values of double differences between ephemerides are within 1 Hz. The single difference between the ephemerides of pseudorange observations

Table 1: The main observations are available for the 5G smart communication base station.

Name	Attribute	Describe
GNSS Clock	Class	Clock class, used to calculate pseudorange observations
Accumulated delta range meters	Observed value	Carrier phase observations
Cn0Db (Hz)	Observed value	Signal to noise ratio
Carrier frequeney (Hz)	Observed value	Carrier frequency
Pseudorange rate meters per second	Observed value	Pseudorange change rate

Table 2: 5G smart communication base station observation double difference error statistics.

Satellite	Doppler double difference (Hz)	Pseudorange double difference (m)
G3	0.562	4454.335
G7	0.507	310.468
G8	0.317	4890.355
G9	0.315	4367.548
G11	0.316	3.344
G14	0.381	4305.128
G16	0.307	3690.258
G21	0.753	4498.947
G22	0.362	26.222
G23	0.411	3698.558
G25	1.138	37.135
G26	0.306	3691.353
G27	0.308	3965.124
G29	0.505	82.488
G31	0.306	3690.334
G32	0.292	5.055

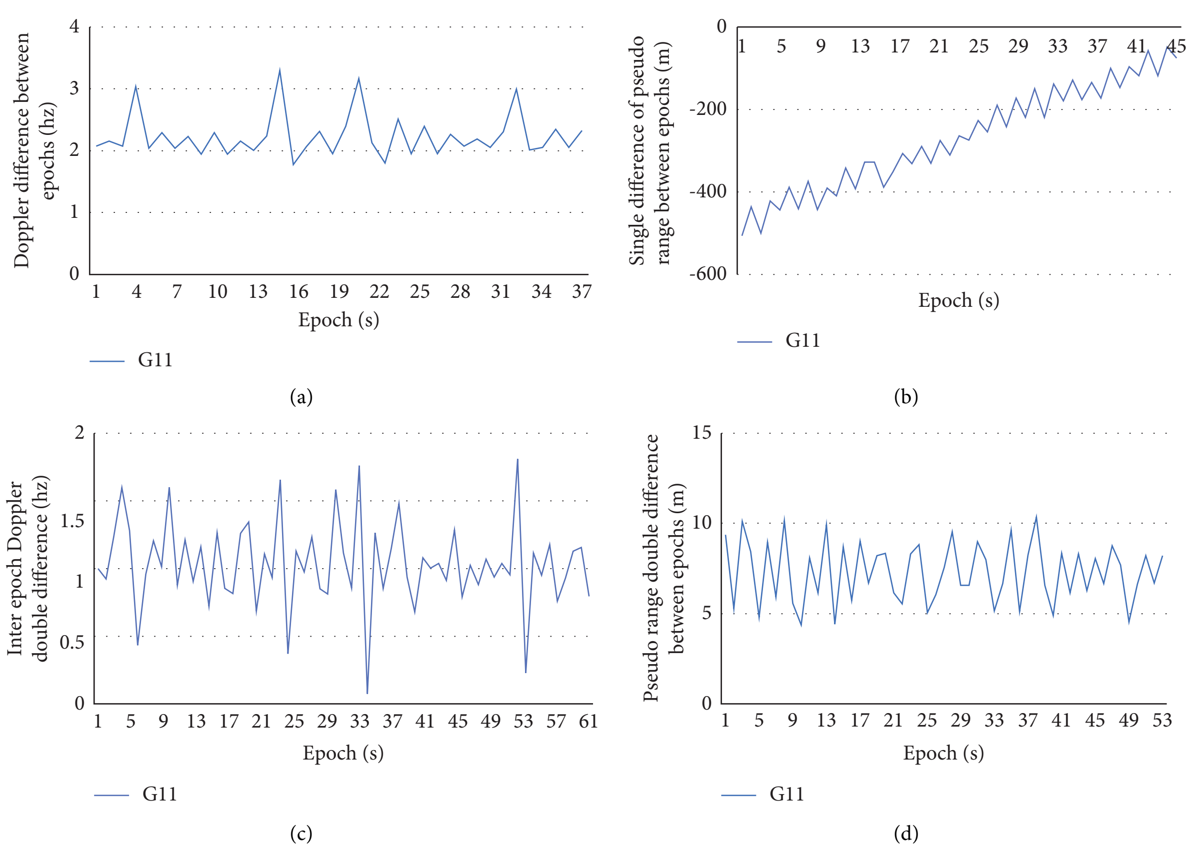

Figure 4: Doppler difference and pseudorange difference between ephemeris elements of the G11 satellite. (a) Doppler single difference. (b) Pseudorange single difference. (c) Doppler double difference. (d) Pseudorange double difference.

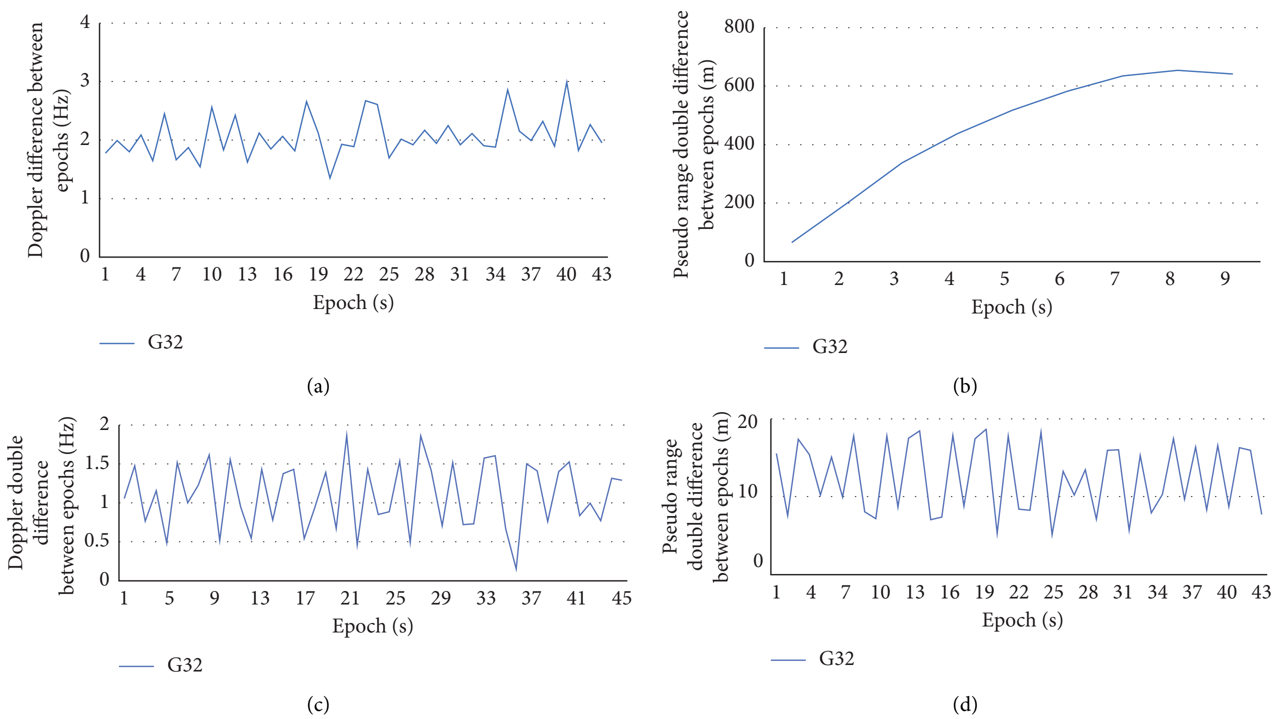

Figure 5: Doppler difference and pseudorange difference between ephemeris elements of the G32 satellite. (a) Doppler single difference. (b) Pseudorange single difference. (c) Doppler double difference. (d) Pseudorange double difference.

varied smoothly, and the absolute value of the double difference between the ephemerides did not exceed 25 m.

Figure 6 shows single and double differences between Doppler and pseudorange observations of the G22 satellite, calendar element by calendar element. It can be seen that there is no jump in Doppler values; 99.9% of the absolute values of single differences between Doppler values are within 2 Hz, and most of the absolute values of double differences between ephemerides are within 1 Hz. For most of the pseudorange observations, the single difference between ephemerides varied smoothly, but there were frequent jumps between 1000 and 3000 ephemerides, and the absolute value of the double difference between ephemerides exceeded 200 m, which was larger than the broad value.

Figure 7 shows single and double differences between Doppler and pseudorange observations of the G23 satellite on an ephemeris-by-ephemeris basis. It can be seen that there are seven Doppler single differences greater than 2 Hz between 7000 and 11000 epochs and many double differences greater than 2 Hz between 10 000 and 11 000 epochs, while pseudorange observations have a large coarse difference of 300 km jumps between 8000 and 9000 epochs.

The GPS L1 single-frequency data were smoothed with a satellite cut-off altitude angle of 15° and a signal-to-noise ratio reading of 30 dB-Hz, and smoothing windows of 50, 100, 120, and no smoothing were selected for comparison. After the test, accuracy was significantly improved, and the test results are shown in Table 3.

As can be seen from Table 3, RMS values of smoothed single-point localization results become smaller in all directions, and the accuracy of smoothed window 100 improves by 11.0% in the *E* direction, 10.0% in the *N* direction, and 4.0% in the *U* direction over smoothed window 50 results; the accuracy of smoothed window 100 improves by 67.9% in the *E* direction, 64.8% in the *N* direction, and 65.5% in the *U* direction over unsmoothed results. Although the solution accuracy of smoothed window 120 is improved over that of smoothed window 100, improvement is limited.

As can be seen from Table 4, pseudorange observations contain coarse errors when data are not preprocessed, which leads to no results in data solution, and after star picking, the data solution rate reaches 100%, which verifies the necessity of coarse error removal before smoothing pseudorange. In summary, it is especially important to remove the Doppler jump and deal with the pseudorange observation jump before Doppler smoothing pseudorange, and Doppler jump and the pseudorange jump are not related, so they should be handled separately in coarse error rejection. If the wrong value is introduced, it will affect smoothed pseudorange observations and continue to affect subsequent localization results on an epoch-by-epoch basis. Based on the abovementioned analysis, 0.9 Hz is selected as the reading value for the double difference between Doppler ephemeris elements, and 15 m is selected as the reading value for the double difference between pseudorange ephemeris elements.

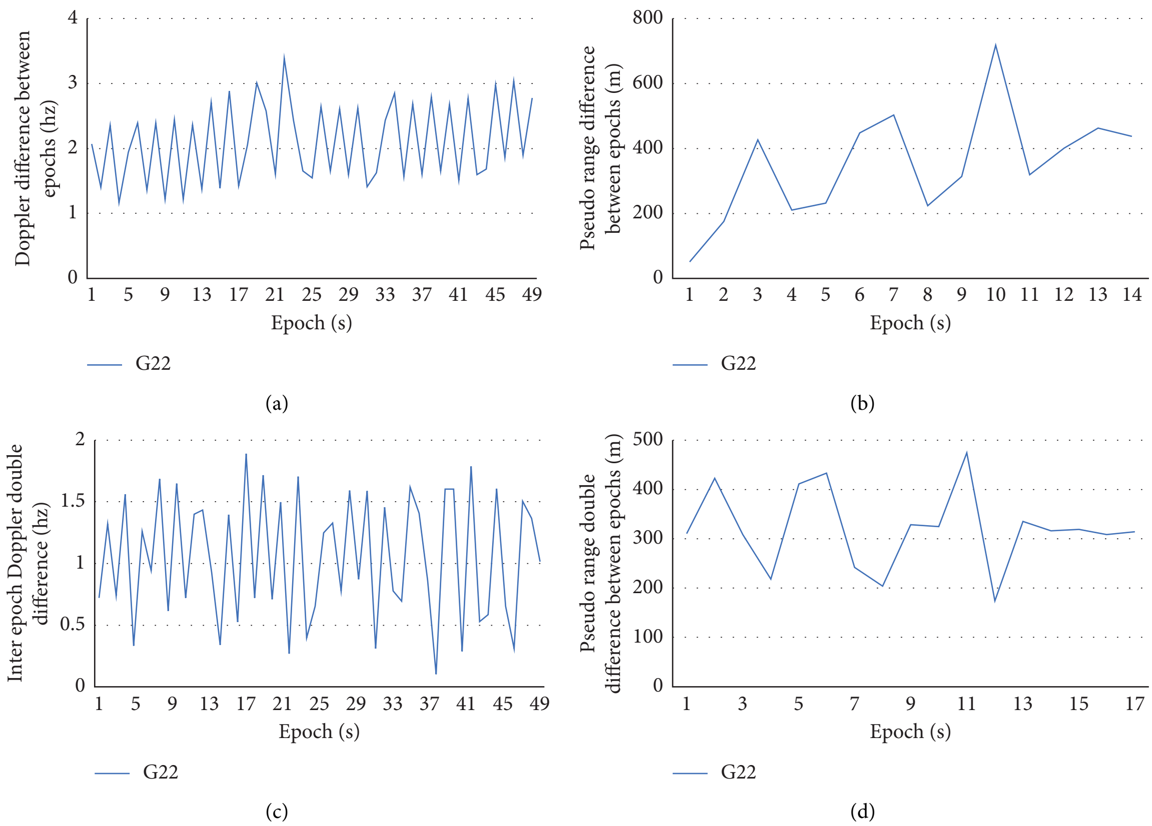

Figure 6: Doppler difference and pseudorange difference between ephemeris elements of the G22 satellite. (a) Doppler single difference. (b) Pseudorange single difference. (c) Doppler double difference. (d) Pseudorange double difference.

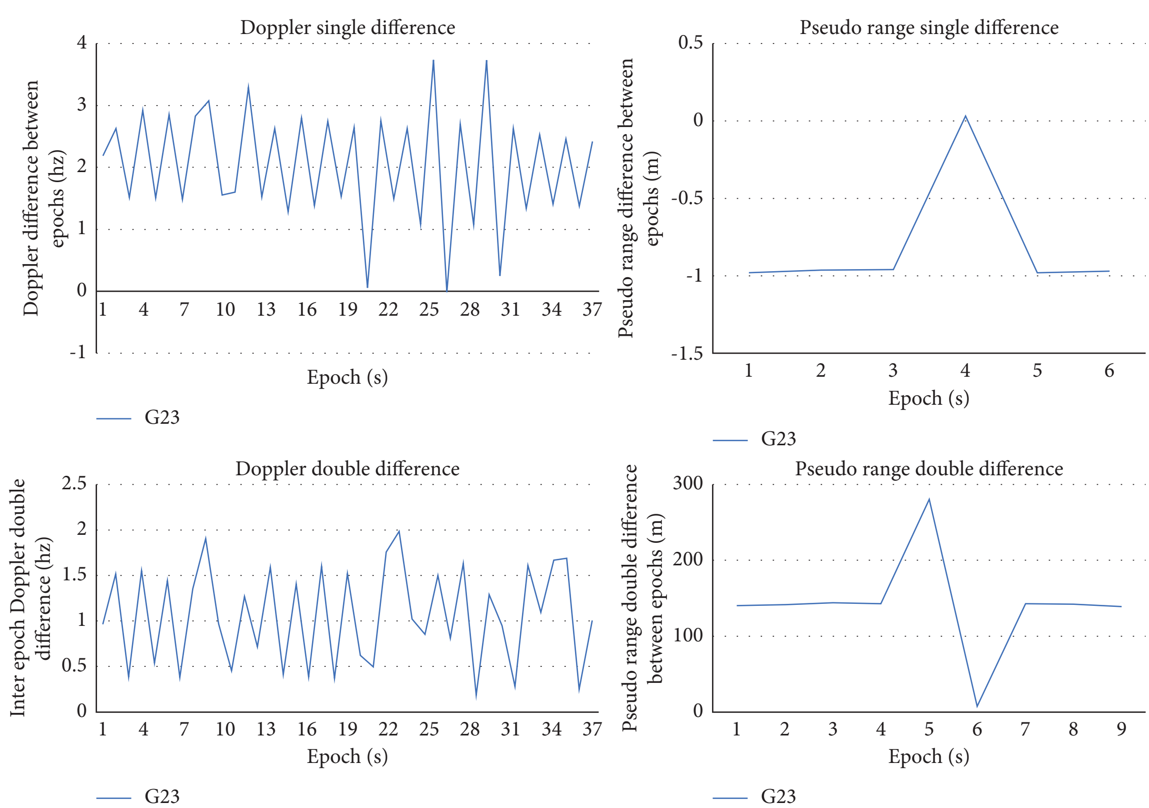

Figure 7: Doppler difference and pseudorange difference between the ephemerides of the G23 satellite. (a) Doppler single difference. (b) Pseudorange single difference. (c) Doppler double difference. (d) Pseudorange double difference.

Table 3: 5G smart communication base station smoothing pseudorange positioning outside conformal accuracy (RMS) statistics.

RMS	N (m)	E (m)	U (m)
Unsmoothed	2.28	1.95	4.44
Smooth window 50	0.83	0.77	1.72
Smooth window 100	0.72	0.69	1.54
Smooth window 120	0.71	0.66	1.49

Table 4: Statistics of data solving rate.

Smooth window	Primitive epoch	Solve epoch	Solution rate (%)
Unsmoothed	13200	13185	99.88
Smooth window 50	13200	13200	100
Smooth window 100	13200	13200	100
Smooth window 120	13200	13200	100

5. Conclusion

This paper first introduces the principle of GNSS pseudorange single-point positioning, then introduces carrier phase smoothing pseudorange and Doppler smoothing pseudorange according to the poor quality of smartphone pseudorange observations, and compares and analyzes the three strategies of pseudorange single-point positioning, pseudorange single-point positioning after carrier phase smoothing, and pseudorange single-point positioning after Doppler smoothing. The experimental results show that Doppler smoothing pseudorange can improve the positioning accuracy. When the smoothing window is 100, the pseudorange single-point localization strategy with carrier phase smoothing improves the localization results by 67.9% in the E direction, 64.8% in the N direction, and 65.5% in the U direction compared with the pseudorange single-point localization strategy without carrier phase smoothing. The original pseudorange observations with carrier phase and Doppler smoothing can effectively reduce the noise effect and thus improve accuracy.

Data Availability

The experimental data used to support the findings of this study are available from the corresponding author upon request.

Conflicts of Interest

The authors declare that they have no conflicts of interest.

Acknowledgments

The study was supported by the "National Natural Science Foundation of China (Project Number: 41474020)."

References

[1] L. Wang, Z. Li, N. Wang, and Z. Wang, "Real-time GNSS precise point positioning for low-cost smart devices," *GPS Solutions*, vol. 25, no. 2, pp. 69–13, 2021.

[2] D. Wu, Y. Lei, M. He, C. Zhang, and L. Ji, "Deep reinforcement learning-based path control and optimization for unmanned ships," *Wireless Communications and Mobile Computing*, vol. 2022, Article ID 7135043, 2022.

[3] G. Wang, Y. Bo, Q. Yu, M. Li, Z. Yin, and Y. Chen, "Ionosphere-constrained single-frequency PPP with an Android smartphone and assessment of GNSS observations," *Sensors*, vol. 20, no. 20, p. 5917, 2020.

[4] G. Cai, Y. Fang, J. Wen, S. Mumtaz, Y. Song, and V. Frascolla, "Multi-carrier M-ary DCSK system with code index modulation: an efficient solution for chaotic communications," *IEEE Journal of Selected Topics in Signal Processing*, vol. 13, no. 6, pp. 1375–1386, 2019.

[5] M. Håkansson, "Characterization of GNSS observations from a nexus 9 android tablet," *GPS Solutions*, vol. 23, no. 1, pp. 21–14, 2019.

[6] K. Chandra, A. S. Marcano, S. Mumtaz, R. V. Prasad, and H. L. Christiansen, "Unveiling capacity gains in ultradense networks: using mm-wave NOMA," *IEEE Vehicular Technology Magazine*, vol. 13, no. 2, pp. 75–83, 2018.

[7] X. Li, X. Guo, K. Liu et al., "Single-frequency cycle slip detection and repair based on Doppler residuals with inertial aiding for ground-based navigation systems," *GPS Solutions*, vol. 26, no. 4, pp. 116–211, 2022.

[8] S. Palanisamy, B. Thangaraju, O. I. Khalaf, Y. Alotaibi, S. Alghamdi, and F. Alassery, "A novel approach of design and analysis of a hexagonal fractal antenna array (HFAA) for next-generation wireless communication," *Energies*, vol. 14, no. 19, p. 6204, 2021.

[9] S. Nagi Alsubari, S. N Deshmukh, A. Abdullah Alqarni, N. Alsharif, T. H H Aldhyani, and F. O. Waselallah Alsaade, "Data analytics for the identification of fake reviews using supervised learning," *Computers, Materials & Continua*, vol. 70, no. 2, pp. 3189–3204, 2022.

[10] M. Pepe, D. Costantino, G. Vozza, and V. S. Alfio, "Comparison of two approaches to GNSS positioning using code pseudoranges generated by smartphone device," *Applied Sciences*, vol. 11, no. 11, p. 4787, 2021.

[11] Q. Liu, C. Liu, and Y. Wang, "Integrating external dictionary knowledge in conference scenarios the field of personalized machine translation method," *Journal of Chinese Informatics*, vol. 33, no. 10, pp. 31–37, 2019.

[12] B. Smeresky, P. Abell, M. Fries, M. Hankey, and J. M. Trigo-Rodriguez, "Bolide fragment detection in Doppler weather radar data using artificial intelligence/machine learning," *Meteoritics & Planetary Sciences*, vol. 56, no. 8, pp. 1585–1596, 2021.

[13] H. Zhou, Z. Li, C. Liu, J. Xu, S. Li, and K. Zhou, "Assessment of the performance of carrier-phase and Doppler smoothing code for low-cost GNSS receiver positioning," *Results in Physics*, vol. 19, Article ID 103574, 2020.

[14] K. Liu, X. Guo, J. Yang et al., "Kinematic ME-MAFA for pseudolite carrier-phase ambiguity resolution in precise single-point positioning," *Sensors*, vol. 20, no. 21, p. 6197, 2020.

[15] J. Paziewski, "Recent advances and perspectives for positioning and applications with smartphone GNSS observations," *Measurement Science and Technology*, vol. 31, no. 9, Article ID 091001, 2020.

[16] M. Pepe, D. Costantino, G. Vozza, and V. S. Alfio, "Comparison of two approaches to GNSS positioning using code pseudoranges generated by smartphone device," *Applied Sciences*, vol. 11, no. 11, p. 4787, 2021.

[17] F. Zangenehnejad and Y. Gao, "GNSS smartphones positioning: advances, challenges, opportunities, and future perspectives," *Satellite Navigation*, vol. 2, no. 1, pp. 24–23, 2021.

[18] Y. Xia, X. Meng, Y. Yang, S. Pan, Q. Zhao, and W. Gao, "First results of BDS positioning for LBS applications in the UK," *Satellite Navigation*, vol. 2, no. 1, pp. 8–19, 2021.

[19] K. Zhang, W. Jiao, L. Wang, Z. Li, J. Li, and K. Zhou, "Smart-RTK: multi-GNSS kinematic positioning approach on android smart devices with Doppler-smoothed-code filter and constant acceleration model," *Advances in Space Research*, vol. 64, no. 9, pp. 1662–1674, 2019.

[20] G. Amponis, T. Lagkas, M. Zevgara et al., "Drones in B5G/6G networks as flying base stations," *Drones*, vol. 6, no. 2, p. 39, 2022.